Published in final edited form as:
Nat Nanotechnol. 2018 June ; 13(6): 496–503. doi:10.1038/s41565-018-0109-z.

A bio-hybrid DNA rotor/stator nanoengine that moves along predefined tracks

Julián Valero[1], **Nibedita Pal**[2], **Soma Dhakal**[2,4], **Nils G. Walter**[2], and **Michael Famulok**[1,3]

[1]LIMES Program Unit Chemical Biology & Medicinal Chemistry, c/o Kekulé Institut für Organische Chemie und Biochemie, University of Bonn, Gerhard-Domagk-Straße 1, 53121 Bonn, Germany

[2]Single Molecule Analysis Group, Department of Chemistry, University of Michigan, Ann Arbor, MI 48109-1055, USA

[3]Center of Advanced European Studies and Research (CAESAR), Ludwig-Erhard-Allee 2, 53175 Bonn, German

Abstract

Biological motors are highly complex protein assemblies that generate linear or rotary motion, powered by chemical energy. Synthetic motors based on DNA nanostructures, bio-hybrid designs, or synthetic organic chemistry have been assembled. However, unidirectionally rotating biomimetic wheel motors with rotor-stator units that consume chemical energy are elusive. Here we report a bio-hybrid nanoengine consisting of a catalytic stator that unidirectionally rotates an interlocked DNA wheel, powered by NTP hydrolysis. The engine consists of an engineered T7 RNA polymerase (T7RNAP-ZIF) attached to a double-stranded (ds)DNA nanoring that is catenated to a rigid rotating dsDNA wheel. The wheel motor produces long, repetitive RNA transcripts that remain attached to the engine and are used to guide its movement along predefined single-stranded (ss)DNA tracks arranged on a DNA nanotube. The simplicity of the design renders this walking nanoengine adaptable to other biological nanoarchitectures, facilitating the construction of complex bio-hybrid structures that achieve NTP-driven locomotion.

Nature provides several examples of highly effective biological motors that consume chemical energy for rotation, movement, or power transmission1. Living organisms require

Correspondence and requests for materials should be addressed to M. Famulok.
[4]Current affiliation: Department of Chemistry, Virginia Commonwealth University, Richmond, VA 23284, USA

ORCID IDs: Julián Valero: 0000-0002-5260-2770
Michael Famulok: 0000-0001-5878-6577

Authors Contributions M. F. and J. V. developed the concepts of interlocked bio-hybrid nanoengines and the walking principle. J. V. performed and designed, with M. F., most of the included studies. M. F. supervised the research project. N. P., S. D., and N. G. W. planned and performed the single molecule fluorescence experiments. All authors discussed the experimental results and contributed to writing the manuscript, with J. V. and M. F. doing the bulk of the writing.

Data availability statement The data that support the plots within this paper and other findings of this study are available from the corresponding author upon reasonable request

The authors declare no competing financial interests.

Additional information
Reprints and permission information is available online at www.nature.com/reprints

Europe PMC Funders Author Manuscripts

motors for essential functions such as cargo transport, cell locomotion and division, chemotaxis, ATP synthesis2, or flagellar movement3, with the latter two consisting of interacting stator and rotor components that generate torque. Despite the complexity of most natural motors, artificial motor systems have been possible to assemble by employing DNA nanostructures4–7, bio-hybrid designs8–10, or based entirely upon synthetic organic chemistry11–13. Apart from synthetic small molecule motors14, however, unidirectionally rotating biomimetic wheel motors with rotor-stator units that consume chemical energy have not yet been described.

Here, we describe a supramolecular bio-hybrid rotor composed of a catalytic stator that unidirectionally rotates an interlocked double-stranded (ds)DNA wheel, powered by the hydrolysis of nucleotide triphosphates (NTPs). The design of the engine consists of a static building block with an engineered T7 RNA polymerase (T7RNAP) fused to a DNA-binding Zn^{2+}-finger (ZIF) motif (T7RNAP-ZIF). T7RNAP-ZIF attaches firmly to a double-stranded (ds)DNA nanoring thus constituting a stator unit that is interlocked with a rigid rotating dsDNA wheel, the rotor-unit, to form a catenane. The wheel motor operates continuously and thereby produces long, repetitive RNA transcripts by rolling circle transcription (RCT). Since this RNA byproduct remains attached to the bio-hybrid nanoengine it can be used to guide the movement of the entire engine along predefined single-stranded (ss)DNA tracks arrayed on a DNA nanotube.

Design, integrity, and characterization of the nanorotor

Integrating T7RNAP as a power generator for our wheel motor offered several design opportunities (Figure 1). First, because torque-generation requires defined stator-rotor interactions, T7RNAP had to be firmly attached to a stationary chassis; otherwise the rotational motion would become undefined, as is the case in classical RCT15 where either the polymerase or the circular template can be regarded as the moving part. Second, interlocking of the rings, each containing a different recognition motif for T7RNAP-ZIF, promotes cooperative binding, reducing the probability of polymerase detachment and thereby boosting processivity. Third, we integrated means for quantification of the motor rotation (Figure 1).

The stator chassis is a 168-base pair (bp) dsDNA circle containing the 10-bp sequence that binds the three Zn^{2+}-finger motif of the Zif268 protein (Figure 1a)16. This sequence was previously used for the site-specific positioning of Zn^{2+}-finger containing proteins on DNA origami17,18. Here, it serves as a high-affinity docking site for a T7RNAP N-terminally fused with Zif268 (T7RNAP-ZIF; Figure S1a). The rotor ring contains a T7 promoter (red) and a sequence that allows hybridization of a complementary molecular beacon (MB, green) to the RNA transcript for fluorescence monitoring of product formation. The assembly of the interlocked catenane was performed as described previously (Figure S1b, S2, Table S1)19. Gel electrophoresis showed that the mechanically interlocked $catenane^{mec}$ migrates slightly faster than the corresponding hybridized $catenane^{hyb}$ (Figure S1c, Cat^{hyb}), consistent with previous observations on similar DNA nanostructures.19–22

The Zif268-fragment of T7RNAP-ZIF binds sequence-specifically to the 168-bp stator ring with a K_d of 1.6 nM, as determined by surface plasmon resonance (Figure S1d), whereas the T7RNAP fragment recognizes the T7 promoter in the 126-bp rotor ring, completing the bio-hybrid nanoengine. *In vitro* transcription using a non-interlocked circular DNA template showed that T7RNAP-ZIF performs just like wild-type (wt)T7RNAP (Figure S1e), thus binding to its corresponding T7 promoter, which dictates the direction of transcription on the circular dsDNA template. Atomic force microscopy (AFM) of the isolated catenane (Figure 1b), T7RNAP-ZIF (Figure 1c), and the assembled nanoengine (Figure 1d; Figure S3,S4) demonstrated the structural integrity of each sample. Most T7RNAP-ZIF molecules co-localize with the catenane, indicating effective complex formation (Figure 1d,e). In contrast, without the ZIF-binding DNA sequence (noZIF-catenane, Figure S1f,i), most mica-deposited T7RNAP-ZIF molecules were washed away, or did not co-localize with catenane molecules (Figure S1i, right panel). MB-fluorescence analysis of the RNA generated *in situ* by the wtT7RNAP (Figure S5) revealed comparable transcription activity (Figure 1f) for the ZIF-containing catenane (ZIF-catenane, Figure 1a), the noZIF-catenane, and the 126-bp ring control containing the MB (Figure S1f,g). Conversely, when using T7RNAP-ZIF, the ZIF-catenane showed a linear increase of RCT during the entire 160 min time course (Figure 1g, blue), whereas the transcription levels of the noZIF-catenane and MB-containing 126-bp ring controls (Figure 1g, red, green) were similar to those of T7RNAP on the ZIF-catenane (Figure 1f). A 126-bp ring lacking the MB-binding site (Figure S1h) showed negligible fluorescence (Figure 1G, black). Increasing amounts of linear dsDNA containing the ZIF motif (Figure S1d) efficiently competed for T7RNAP-ZIF, decreasing RCT levels (Figure S1j, blue) to those of the noZIF-catenane (Figure S1j, red). Transcription rate constants measured at different concentrations of catenane and ring-templates (Figure 1h) confirmed the elevated RCT efficiencies of the ZIF-catenane compared to the controls. Taken together, these results support the formation of the fully functional nanoengine as designed.

Molecular Beacon calibration and RCT kinetics

We next calibrated the MB fluorescence signal using its complementary DNA (cDNA) sequence, plotting fluorescence levels against increasing cDNA concentrations (Figure S6), which allowed to quantify the RNA transcribed from the ZIF-catenane, noZIF-catenane, and MB-ring at 5 and 10 nM template concentrations (Figure S7). This analysis revealed speeds of 0.23 rotations per minute (rpm), or 0.48 nucleotides per second (nt/s), for the ZIF-catenane, 0.08 rpm (0.17 nt/s) for the noZIF-catenane, and 0.11 rpm (0.23 nt/s) for the MB-ring control (Figure S6). The cooperative binding of T7RNAP-ZIF to the ZIF-catenane results in an increased transcription efficiency compared to T7RNAP, the noZIF-catenane, or the MB-ring. The overall reduced transcription rate observed for our circular dsDNA rings has previously been described for other tightly looped DNA rings compared to linear templates23: an elongating T7 RNAP on a highly bent circular DNA template similar to ours shows highly unidirectional processivity over ~8,000 bp, or ~40 and ~60 cycles for the 210-bp and 126-bp rotors, respectively. Together, our data suggest that the stator-bound T7RNAP-ZIF drives the unidirectional rotation of the rotor.

Europe PMC Funders Author Manuscripts

Single Molecule FRET studies

To assess the rotatory motion of individual nanoengines, we conceived a series of single-molecule FRET (smFRET) experiments. The design required labelling24 the non-coding strands of rotor and stator with a donor Cyanine 3 (Cy3) and an acceptor Cyanine 5 (Cy5) FRET pair, respectively. For surface immobilization of the nanoengine, the stator ring was modified with a protruding 5'-biotinylated dsDNA strand (Figure 2a, Figure S8a-c). During the rotation of the rotor over the stator ring, the relative distance between the fluorophores changes periodically, generating an oscillating FRET signal that we monitored using total internal reflection fluorescence microscopy (TIRFM, Figure 2a). The oscillation frequency should reflect the rotational cycle and therefore should help assess an individual nanoengine's rotational frequency. Indeed, smFRET time traces during transcription showed periodic oscillatory FRET signals with donor and acceptor intensities changing in anti-correlated fashion (Figure 2b and Figure S9). Kinetic analysis of the full FRET cycles (Figure 2c, upper right; details provided in Methods), which each entail a dwell time in the high-FRET state (Figure 2c, upper left panel) and one in the low-FRET state (Figure 2c, upper middle panel), yielded an average rotation time of 590 ±87 s (0.10 rpm), consistent with the sum of the low- and high-FRET half cycle dwell times analysed separately (610 ±33 s). The average rpm of 0.10 (0.21 nt/s) determined by smFRET matches within two-fold the value obtained by bulk fluorescence, consistent with the difference in temperature of the two experiments (25 °C and 37 °C, respectively, Figure S8d).

The fraction of DNA nanoengines exhibiting these dynamic FRET transitions was >35% (Figure 2d), attesting to a reasonable assembly yield. This percentage dropped to 2% when T7RNAP instead of T7RNAP-ZIF was used, and was <1% in the absence of NTPs (Figure 2d), with the remaining traces showing either zero or static FRET throughout, demonstrating that unidirectional rotation is enabled only upon T7RNAP-ZIF-based transcription. The T7RNAP transcription control produced a static average FRET signal close to zero, consistent with random Brownian motion of one ring *versus* the other as the FRET pairs can move arbitrarily through the interlocked space in the absence of the ZIF-based stator attachment, with an average distance of 15.9 nm, far beyond the FRET detection range of up to ~10 nm (Figure S10). Similarly, in a T7RNAP-ZIF control experiment without NTP zero FRET trajectories were observed (Figure S11); transition occupation density plots (TODP) of the experiments without and with NTPs illustrate the dynamic transitions only in the latter case (Figure S12).

It was previously found that T7RNAP transcription accelerates with decreasing ring-strain23. We therefore performed smFRET experiments using a 210-bp rotor catenane instead of the 126-bp rotor. Although the average full rotation time of the 210-bp rotor remained almost unchanged (550 ±27 s ≈0.11 rpm, Figure 2c lower panels), the nucleotide incorporation rate was 1.8-fold higher (0.38 nt/s, Figure 2c, lower panels) than that of the 126-bp rotor, as expected. When detected by MB fluorescence the 210-bp rotor catenane similarly showed 2.8-fold faster nucleotide incorporation than the 126-bp rotor (Figure S8e).

In our smFRET traces of both the 126-bp and 210-bp rotors, we observed multiple transitions (Figure S9), representative of repetitive transcription cycles. For the 210-bp rotor,

43% smFRET trajectories showed more than one-and-a-half full transcription cycles before photobleaching, compared to 28% for the 126-bp rotor (Figure S13). This observation supports the notion that dissociation of both ZIF and T7RNAP is negligible within our long observation time window (~20 min). It is also consistent with the known high processivity of an elongating T7RNAP on a highly bent circular DNA template23. This high processivity is likely further enhanced by the tight binding of ZIF with a known dissociation rate constant of 2×10^{-4} s^{-1} (ref. 25). This high processivity reaches far beyond our smFRET observation window of just a few cycles.

The smFRET trajectories showed strikingly gradual, monotonous changes when transitioning from the high- to the low-FRET state and vice versa (Figure 2e, Figure S14). The probability densities of the resulting transition times were not single-exponential, suggesting that more than one rate constant arises from the underlying molecular processes (Figure 2f). This observation fits the facts that a single NTP incorporation itself involves multiple steps, including DNA unwinding, NTP binding, a conformational change upon pyrophosphate release, and enzyme translocation; and that it may take multiple NTP incorporations to move the fluorophores out of or into FRET distance. To extract the number of steps involved, we fitted the probability densities with Gamma functions and obtained 2.3 steps for the 126-bp rotor and 2.6 steps for the 210-bp rotor, with transition times of ~1 s in both cases (Figure 2f, Table S2). The similar transition rates and general symmetry of the high-to-low and low-to-high FRET transitions (Figure S14) support that they reflect the action of a processive T7RNAP rather than mere Brownian rotation. Given that our full cycle times predict an NTP incorporation rate of ~0.2-0.5 s^{-1}, this leaves two possible interpretations – our Gamma function steps represent the sub-steps of a single NTP incorporation, or elongation is fast where the fluorophores leave and enter FRET distance but is slowed at other segments of the rotation, such as when topological or sterical stress is encountered. Given that previous measurements of T7RNAP on similarly bent, uncatenated substrates found an incorporation rate of ~4 nt/s at 37 °C23, we favour the model wherein our Gamma function steps relate to the number of NTP incorporations needed to bring the fluorophores out of or into FRET range, and an occasional topological strain release slows the cycle elsewhere. It may also be possible that the donor fluorophore and the promoter segment slow down the rotation, explaining the slow progress in the high and low FRET states. Taken together, our single-molecule results strongly support the NTP-fuelled unidirectional rotation of the rotor in the fully assembled DNA nanoengine.

Nanoengine-based walker design

Transcription by T7RNAP-ZIF generates a long, repetitive RNA transcript encoded by the rotor ring template, which remains bound to the nanoengine and can be harnessed to guide the movement of the nanoengine along predefined DNA tracks. We used the 210-bp ring as the rotor and added an ssDNA-branch with two different domains (Figure 3a, linear red, green,Figure S15) to the stator ring, to allow hybridizing the nanoengine to two distinct complementary ssDNAs, Step1 and Step2 (Figure S16). The path consists of a rigid DNA-origami nanotube containing different protruding ssDNA sequences serving as steps for hybridization of the nanoengine at various stages of transcription (Figure 3b,c, Figure S17,S18, Table S3). Spatiotemporally controlled strand-displacement reactions and

hybridization of the RCT-generated RNA to the protruding steps are expected to guide the motion of the nanoengine along the path. Prior to transcription, the nanoengine preferentially hybridized to Step1 (Figure 3b, red). Upon transcription, the growing RNA strand is expected to displace it from Step1 by forming a thermodynamically more stable DNA/RNA heteroduplex over the entire Step1 sequence (Figure 3b,c, red/blue). As transcription proceeds, the growing RNA can eventually reach the intermediate Step(s) (iStep). Once a sufficient length of RNA is produced, the nanoengine finally is expected to reach Step2 (Figure 3c), located 120 nm from Step1. iSteps serve as additional anchoring points that assist in guiding the nanoengine along the path, thereby endowing it with processivity. To monitor this directed locomotion, we labelled the 5'-position of the catenane's single-stranded sticky end with TAMRA (Fc, Figure 3b,c). Accordingly, when reaching the quencher-labelled (Qc) Step2 the Fc fluorescence is quenched (Figure 3d, red). By contrast, fluorescence remained unchanged (Figure 3d, blue) both in the non-transcription control and in a control where the catenane was hybridized to Step2 by blocking Step1 (Figure 3d, green).

In parallel, the iStep was labelled with a Cy5 fluorophore (Fi) quenched by a complementary oligonucleotide (comp-iStep) bearing the quencher BHQ-3 (Qi). RNA hybridization displaces comp-iStep Cy5 and fluorescence increases (Figure 3e, red) to the level of a control experiment lacking comp-iStep (Figure 3e, blue). The fluorescence signal of the non-transcription control remained quenched (Figure 3e, green).

Preferential binding of the catenane to Step1 prior to transcription was further confirmed by high-resolution (HR)-AFM (Figure 3f, Figure S19). When mimicking the presence of the transcribed RNA by adding a release ODN (RO) that blocks Step1, the catenane selectively hybridized to Step2 (Figure 3g, Figure S19). Similarly, AFM analysis after transcription showed the catenane positioned on Step2 (Figure S20), consistent with the fluorescence experiments (Figure 3d,e).

Walking of the nanoengine

To investigate binding of the RCT-produced RNA to the iSteps, we assembled a path containing three iSteps located ~5, 48, and 177 nm from Step1. By displacing biotinylated complementary iSteps (bio-comp-iSteps) that could be detected by tagging with streptavidin-coated quantum dots (Qdots), we were able to monitor RNA attachment to the different iSteps by AFM. The fraction of iSteps occupied with Qdots should decrease gradually during RCT as the transcribed RNA displaces the bio-comp-iSteps (Figure 4a). Before transcription, an average of ~51% of all available positions had a Qdot attached (Figure 4b), consistent with previously reported efficiencies26. The distinct positioning of the iSteps allowed their discrimination, facilitating the assessment of bio-comp-iStep attachment at each site. AFM analysis of the path before and after transcription revealed efficient displacement of each bio-comp-iStep upon transcription, as visualized by the absence of Qdot-tagging (Figure 4b,c). By counting the number of attached Qdots for each iStep at different time-points we verified that Qdot occupancy progressively decreased during transcription (Figure 4d, Figure S21-S25, Tables S4,S5), but remained stable in the

absence of the catenane walker (Figure 4e, Figure S26-S29). Similar results were obtained with the 126-bp rotor catenane walker (Figure S21b-d, Figure S30-S33).

Each iStep was then labelled with a different fluorophor (Figure 4f) to determine the half-lives (τ) for the RNA hybridization to each individual iStep by progressive release of quencher-labelled comp-iSteps (Figure 4g). The τ-values were 25 ±4 min (iStep1), 32 ±6 min (iStep2), and 40 ±7 min (iStep3), consistent with the expectation that the nanoengine directionally walks from one end to the other. In contrast, a control path lacking Step1 and Step2 with the three iSteps equidistantly positioned at 86 nm (Figure 4h,i) showed identical half-lives of 36 ±11 min for all iSteps, reflective of the random attachment of the RCT transcript upon loss of spatiotemporal control due to diffusion of the nanoengine in solution. These results confirmed progressive and highly processive walking of the nanoengine only if initially attached to Step1.

Walking kinetics and processivity

To further study the nanoengine's kinetics and processivity, we assembled tracks that contained a single iStep at varying positions between the two Steps (Figure 4j). The catenane, all iSteps, and Step2 were labelled with fluorophors and quenchers, respectively, as before (see Figure 3b), to monitor τ of the Step1→2-transition and the RNA binding to the iSteps. We first assembled paths A and B with distances between Step1 and Step2 of 86 nm and 243 nm, respectively. In both paths, the distance between Step1 and the iStep was 48 nm. τ of the Step1→2-transition was ~40% slower in path B than in A (half-life ratio $\tau_{(B/A)}$~1.4, Figure 4k), whereas the iSteps were reached almost simultaneously with $\tau_{(B/A)}$ close to 1 ($\tau_{(B/A)}$~1.1). In paths C and D, Step 2 was at the same distance from Step1 but the iSteps were placed 19 nm and 219 nm from Step1. Here, $\tau_{(D/C)}$ for the Step1→2-transition was ~1.0, while the comp-iStep displacement was 30% slower for path D than for C ($\tau_{(D/C)}$~1.3). These ratios are consistent with the expected dependence of walker kinetics on the distance between steps, strongly supporting processive nanoengine walking rather than detachment and random diffusion to another path.

For the Step1→2 transition, paths C and D showed average half-lives of τ_C = 21 ±11 and τ_D = 22 ±10 min, whereas the half-lives for reaching the iStep were τ_C = 32 ±10 and τ_D = 43 ±13 min. The average Step1→2-transition speed in these paths was ~0.2 nm×s^{-1}. Although still slower than the biological motors kinesin or dynein, the nanoengine belongs to the fastest DNA nanowalkers described so far27–31. The slower kinetics for RNA hybridization to the iSteps compared to the Step1→2-transition may be due to differences in the kinetics of strand displacement and hybridization. RNA binding to the iSteps involves displacement of the quencher-labeled comp-iStep, a process that can considerably slow down the kinetics32. Strand-displacement kinetic control experiments independent of RCT and the relative positioning of the catenane and the steps on the path (Figure S34a) showed that the average half-life for the Step1→2-transition was 0.7 ±0.2 min, whereas the displacement of comp-iStep from iStep was ~10-fold slower (6.5 ±1.7 min, Figure S34b,c). These data support the faster kinetics observed with the nanoengine for the Step1→2 transition compared with the displacement of comp-iStep from iStep. The hybridized comp-iStep only

serves the purpose of tracking the nanoengine's walking. In absence of comp-iStep, RNA binding to the iSteps should occur before the walker reaches Step2.

To study the kinetics and processivity of RNA hybridization to the iStep without the influence of Step2 we assembled paths ΔC and ΔD lacking Step2. The half-life kinetics of comp-iStep displacement in path ΔD was ~70% slower than in path ΔC (Figure 4k, green; $\tau_{(D/C)}$~1.7, $\tau_{\Delta C}$ = 38 ±8 and $\tau_{\Delta D}$ = 66 ±24 min). Due to its proximity to the iStep, Step2 in path D can act as an anchoring point for catenane walker hybridization, synergistically favouring the RNA interaction with the corresponding iStep. These results indicate that the relative positioning of Steps 1 and 2, as well as the location and number of iSteps, can be used to rationally modulate the nanoengine's walking kinetics and processivity.

Conclusion

The nanoengine described here constitutes a unidirectionally rotating molecular motor fuelled by chemical energy that employs an unprecedented autonomous walking mechanism. Its guided walking depends on interlocking of the stator with the rotor ring to allow its free movement during RCT on the one hand, and mechanical anchoring of the entire nanoengine to the programmable path on the other. The straightforward design of this nanoengine differs from synthetic walkers to date12,33, including molecules that walk step by step along predefined tracks34, convert light35, electricity36, fuel- /antifuel inputs37–39, or cleavage energy40,41 into unidirectional motion, or transmission of force42. Our walker is among the fastest artificial molecular walkers described so far43–46. A compelling feature of the design is the fact that a multistep path, once taken, cannot be used a second time, driving directionality. Unlike 'burnt-bridges' walkers where used steps are irretrievably destroyed28,40,41,47, however, our design retains the potential to regenerate its steps after RNA hydrolysis; a property attractive for designing future walkers on prescriptive landscapes to study, for example, swarm-like behaviour on the nanoscale.

The continuous, unidirectional rotation fuelled by triphosphate hydrolysis and the rotor/stator design also sets our bio-hybrid rotor apart from rotors generated by organic synthesis14,36 or DNA nanotechnology7,37,48. Random Brownian motion usually drives the latter, and unidirectional rotation is achieved by selective blockade of the reverse direction. These rotors thus cannot exert torque. We foresee that further optimization of the nanoengine will improve efficiency, speed, and processivity, to approach that of natural protein rotors and walkers. Already our nanoengine combines a multitude of features that we anticipate will facilitate the creation of nanoscale robots capable of performing ever-more sophisticated tasks.

Methods

Buffer systems

1x TAE buffer: 40 mM Tris·HCl, 20 mM AcOH, 1mM EDTA at pH 8.3.

1x DNA buffer: 10 mM Tris·HCl, 50 mM NaCl, 10 mM $MgCl_2$ at pH 7.5.

1x origami buffer: 5 mM Tris·HCl, 1 mM EDTA, 18.5 mM $MgCl_2$ at pH 7.9.

1x ligase buffer: 40 mM Tris·HCl, 10 mM $MgCl_2$, 10 mM DTT, 5 mM ATP at pH 7.8.

WAX buffer A: 20 mM Tris·HCl at pH 9.0.

WAX buffer B: 20 mM Tris·HCl, 1 M NaCl at pH 9.0.

5x transcription buffer: 200 mM Tris·HCl (pH 7.9 at 25 °C), 50 mM DTT, 50 mM NaCl and 10 mM spermidine.

Oligodeoxynucleotides

ODNs used for rings and catenane assemblies were purchased from Ella Biotech GmbH (HPLC purified). ODN staples used for the assembly of the DNA origami nanotube were purchased from Eurofins Genomics GmbH (“High purity salt free [HPSF]” grade) and the M13mp18 scaffold from Tilibit GmbH.

Assembly of 126-bp and 210-bp rotor rings

The oligonucleotides (4 μM) used for the assembly of the rings (see Figure S1 and Table S1) and NaCl (40 mM) in 1x ligase buffer were annealed from 60 °C to 15 °C over 75 min. Ligase (1 μl/100 μl, 10 U) was added and ligated over night at 15 °C. The products were purified by HPLC and concentrated using Amicon Ultra-30K centrifugal filters.

Assembly of partial ¾-168-bp stator rings

The partial ¾-168-bp stator rings containing all ODNs for the different stator rings (See Figure S1 and Table S1) except the threading-ODN was assembled and purified as described for the rotor rings.

Synthesis of catenanes

The assembly of the DNA catenanes described in this work was performed as previously reported19. Briefly, one equivalent of rotor ring was mixed with 1.1 equivalents of threading ODN (in 1x DNA buffer and 1x ligase buffer) and threaded at 4 °C for 1 h. Following the ¾-168-bp stator ring (1.3 equivalents) was added, allowed to hybridize for 15 min before ligase (2 μl/100 μl) was added and ligated for 4 h at 15 °C. To convert the hybridized catenane (Cat^{hyb}) to the mechanically interlocked catenane (Cat^{mec}) (see Figure 1A), first 5 equivalents of “RO-rotor” were added together with more ligase (0.5 μl/100 μl) and incubated for 30 min at 15 °C before 10 equivalents of “RO-stator” were added (see Supplementary Figure 1). The sample was incubated for 4 h at 15 °C, purified by HPLC and concentrated using Amicon Ultra-30K centrifugal filters.

HPLC purification of rings and catenane nanostructures

Rings and other catenane precursors were purified by weak anion exchange HPLC using an isocratic gradient from 0 to 0.5 min at 20% of WAX B buffer and then from 45% to 65% in 20 min (0.8 mL/min flow, column TSKgel DEAE-NPR 4.6 mm x 35 mm (TOSOH)). Catenane structures were similarly purified using an isocratic gradient from 0 to 5 min at 55% of WAX B buffer and then increase the gradient until 62% from 5 to 25 min (0.5 mL/min flow, column TSKgel DNA-NPR 4.6 mm x 75 mm [TOSOH]).

T7RNAP-ZIF protein expression and purification

T7RNAP-ZIF protein was expressed in *Escherichia coli* (Strain BL21 DE3) using the plasmid pQE80-HT-zf-T7-RNAP (H=HisTag; T=TEV; zf=268zif; T7-RNAP= T7 RNA polymerase). Pre-culture was performed by overnight incubation at 37 ºC, using 200 mL of LB medium with 50 μg/mL kanamycin. The solution was then diluted to an OD_{600} of 0.4 (1:10) and when cells reached the mid log phase (OD_{600} ~0.6), IPTG was added to a final concentration of 0.5 mM. Cells were incubated at 37 ºC during 4h for expression, collected by centrifugation (4000 rpm) and stored at -80 ºC or resuspended in 15 mL of lysis buffer (50 mM Tris, pH 7.8 at 4 ºC, 300 mM NaCl, 10% glycerine, 20 mM imidazole and 1 mM $ZnCl_2$). Subsequently, cells were disrupted (French press, 1000 psi max., two rounds), centrifugated at 4 ºC (20000 rpm, 20 min) and the supernatant was incubated with 1.5 mL of Ni-NTA agarose equilibrated bead matrix (Machery Nagel, Düren, Germany) for 30 min and washed 3 times with the lysis buffer. T7RNAP-ZIF construct was expressed with N-terminal His6-tags for its subsequent purification by affinity chromatography (washing 2 times and elution with elution buffer (lysis buffer containing 250 mM imidazole) prior incubation with TEV protease to remove the His6-tag (and consequent reverse Ni-NTA chromatography to remove the His-tag). Finally, size exclusion chromatography (SEC) purification of the sample was performed using a Superdex 200 column (GE Healthcare Life Sciences), fractions were collected and the buffer exchanged by dialysis (Slide-A-Lyzer™ Dialysis Cassettes, 10K MWCO) to storage buffer (50 mM Tris, pH 8.0 at 4 °C, 0.1 mM EDTA, 1 mM DTT, 0.05% (w/v) CHAPS, 50% (v/v) glycerol).

Surface plasmon resonance (SPR) measurement

BIAcore 3000 equipment was used to perform the SPR measurements. Streptavidin (SA) sensor chips (GE Healthcare Life Sciences) were used to immobilise the corresponding biotinylated ODN (see Supplementary Figure 1) containing the binding sequence for 268Zif protein. To this end, 10 μL injection of the dsDNA (50 nM in 1x DNA buffer) followed by an additional 10 μL injection of the complementary ssDNA. Typically, 300-500 resonance units (RUs) of this ODN were immobilized on the chip surface. Different concentrations of T7RNAP-ZIF ranging from 32 nM to 300 nM were injected (200 μL injection of protein in binding buffer: 50 mM HEPES, 50 mM NaCl, 5 mM $MgCl_2$, 20 μM $ZnCl_2$, 2 mM DTT, 0.05% (w/v) Tween) in kinject mode with a contact time of 600s for the association and additional 600s for the dissociation, followed by a direct injection of 20 μL of 0.1% (w/v) SDS solution, with a constant flow rate of 20 μL/min. Dissociation and association kinetic constants (k_{off} and k_{on}, respectively) as well as K_d equilibrium constant were assessed using the Biacore evaluation software.

Molecular beacon fluorescence experiments

To monitor the transcription, real-time fluorescence assays with a molecular beacon were performed. The corresponding DNA template was incubated at different concentrations (typically 5 or 10 nM) with 31.7 μL of $MgCl_2$ (30 mM), 38 μL of a mastermix containing 2.5x transcription buffer, 5 mM NTPs, RNAsin (1:20 v/v), T7RNAP-ZIF (64.5 nM) and 1.5 μM of the molecular beacon (MB) in a total volume of 95 μL. This volume was split in three samples of 30 μL each, loaded in a 384 well plate (Greiner Fluotrac™ 200, 384 well plate)

and the FAM fluorescence (Ex: 491 nm, Em: 521 nm) was measured in a Enspire 2300 plate reader (Perkin Elmer) every 3 min at 37 ºC during 3 h.

Calibration of the molecular beacon

As described for the molecular beacon fluorescence experiments, different concentrations of the JVgmblong_RO ODN (replacing the DNA ring and catenane templates) were mixed with the master mix containing the molecular beacon and the resulting fluorescence was recorded over time in a Enspire 2300 plate reader (see section above for experimental details). JVgmblong_RO is fully complementary to the molecular beacon, thus allowing the hairpin to open which results in an increase of the fluorescence signal. Linear fitting of the fluorescence intensity versus the ODN concentration yielded the corresponding calibration curve for the molecular beacon (See Figure S5) used for assessing RNA concentration during rolling circle transcription.

Sample preparation for smFRET study

Fluorescently labelled nanoengines with protruding 5′-biotinylated dsDNA were immobilized through a biotin−streptavidin interaction onto a quartz slide with a microfluidic channel. The steps of surface functionalization and the construction of the microfluidic channel are described elsewhere.49 An enzymatic oxygen scavenger system (OSS) containing (at 1x) 50 nM protocatechuate-3,4-dioxygenase (PCD), 5 mM protocatechuic acid (PCA), and 2 mM Trolox (6-hydroxy-2,5,7,8-tetramethylchroman-2-carboxylic acid) was added to the imaging buffer to minimize photobleaching and photoblinking of the fluorophores50. Before immobilizing the nanoengines on the quartz slide, the sample was incubated at 37 ºC for 30 min with a 3-fold excess of T7RNAP-ZIF over catenane (catenane:T7RNAP-ZIF = ~0.6:1.7 nM) without rNTP for optimal binding of T7RNAP-ZIF to the catenane. After injecting the nanoengine (catenane/T7RNAP-ZIF complex) into the microfluidic channel, excess unbound T7RNAP-ZIF was washed away by flushing with ~300 μL buffer containing 1x TAE-Mg^{2+} buffer (40 mM Tris base, 20 mM acetic acid, 1 mM EDTA, 12.5 mM $MgCl_2$, pH 7.5) and 1x OSS. Following the washing step, a transcription mixture containing 2.0 mM of each rNTP (i.e., GTP, ATP, CTP, UTP), 1x transcription buffer, RNasin© Ribonuclease Inhibitor [40 U], 25 mM $MgCl_2$, 1x OSS and 5% (v/v) DMSO to conformationally relax the DNA double helices) was injected and incubated for 3 min before collecting Total Internal Reflection Fluorescence Microscopy (TIRFM) movies. All data were collected at ~25 ºC.

Monitoring the rotation of individual nanoengines by smFRET using TIRFM

TIRFM was employed to monitor the rotation of each nanoengine through smFRET. The particulars of the TIRFM instrumental set-up are described elsewhere.51–53 Briefly, a 532 nm green laser (CrystaLaser, CL532-050-L) and a 638 nm red laser (Coherent, 1069415/AR) were used to excite Cy3 and Cy5 molecules, respectively, at ~5.0 mW. The presence of Cy5 was confirmed by directly exciting with the red laser at 638 nm for a brief period at the very beginning and the end of each movie. The emitted fluorescence was collected through a 60x 1.2 NA water immersion objective from Olympus (Olympus UplanApo). The fluorescence emission was split into donor and acceptor signals by pairs of dichroic mirrors and reflective mirrors (Thorlabs) and projected onto the two halves of an

Europe PMC Funders Author Manuscripts

intensified charged-coupled device (ICCD, I-Pentamax, Princeton Instruments). Fluorescence time traces were collected as movies using the ICCD at 100 ms time resolution. The typical duration of data collection was ~20 min. The data acquisition started 3-4 min after the injection of transcription mixture into the slide to allow the oxygen scavenger system sufficient time to remove molecular oxygen introduced through the perturbation of injection. We chose to pursue continuous observation in our experiments to detect any significant disengagement of the nanoengine from its template, which should lead to spurious fluctuations of either the FRET signal or FRET state dwell time. The upper limit of our observation window arose from inevitable photobleaching of the fluorophores, which was reduced by lowering the excitation laser power to ~5 mW, as low as possible without inappropriately deteriorating either the signal-to-noise ratio or the time resolution needed to distinguish the two quite similar FRET values.

Analysis of smFRET data

Intensity time traces were generated from the recorded movies using IDL (Research Systems, Inc.) and analysed further using MATLAB scripts as described.54 Dwell times in the high- and low-FRET states were extracted from the single-molecule intensity time traces by identifying the transition points from low- to high-FRET and vice versa within the error limit of one frame (0.1 s) using hidden Markov model fit. The cumulative distributions of dwell times in the low- and high-FRET states were fitted with single-exponential functions to extract the most probable dwell times, whereas the cumulative distribution of dwell times for the full transcription cycle was fitted with a Gamma function using MATLAB. The time over which the transitions between the two FRET states occurred were extracted and the probability density of these transition times fitted with a Gamma function using MATLAB to reveal the number of intermediate steps. The probability density describes the likelihood of a random variable (the transition time in this case) to fall within a particular range of values. A Gamma function yields a shape factor corresponding to the number n of irreversible states and dwell times in each state.55 All dwell times were corrected for the limited time window of data collection/trajectory truncation as described56 (Supplementary Table 2).

Assembly of the DNA catenane walker

One equivalent of rotor ring was mixed with 1.1 equivalents of threading ODN (in 1x DNA buffer and 1x ligase buffer +10 mM $MgCl_2$) and threaded at 4 °C for 1 h. Simultaneously, the ¾-168-bp stator ring (1.3 equivalents in 1.5x DNA buffer and 1x ligase buffer) was incubated with the Blocker_Rc2c ODN (1.5 equivalents) at 40 ºC for 1h and then incubated at 4 ºC for 5 min before adding it to the rotor ring solution. The mixture was incubated for 15 min before adding the ligase (2 μl/100 μl) and then ligated for 4 h at 15 °C. To convert the hybridized catenane (Cat^{hyb}) to the mechanically interlocked catenane (Cat^{mec}), first 5 equivalents of “RO-rotor” were added together with more ligase (0.5 μl/100 μl) and incubated for 30 min at 15 °C before 10 equivalents of “RO-stator” were added. The sample was incubated for 3 h at 15 °C. Finally, the RO-Blocker_Rc2c (3 equivalents) was added in order to release the Blocker_Rc2c ODN from the ss-region of the stator, incubated for 30 min, purified by HPLC and concentrated using Amicon Ultra-30K centrifugal filters.

Design and assembly of the six-helix bundle DNA origami

The six-helix bundle DNA origami was designed using the 2.2.0 version of caDNAno57. For the assembly, the DNA M13mp18 scaffold (7429 bp, 20 nM) was mixed with the corresponding DNA staples at 200 nM concentration each, in 1x TAE buffer (40 mM Tris, 20 mM acetic acid, 1 mM EDTA, pH 8), 5 mM NaCl and 20 mM $MgCl_2$. The mixture was subjected to thermal annealing in a Nexus thermocycler (Eppendorf), from 80 to 65 ºC at 1 ºC per min and from 65 to 20 in steps of 20 min/ºC. The samples were purified following the PEG precipitation protocol described previously58. Briefly, samples were mixed 1:1 (v/v) with precipitation buffer (15% PEG 800 (w/v) (Carl Roth), 5 mM Tris, 1 mM EDTA and 505 mM NaCl) and spun at 16000 g for 25 min at room temperature using a microcentrifuge (Eppendorf 5424R, Hamburg, Germany). Then, the supernatant was discarded and the pellet containing the DNA origami nanotubes dissolved in 1x origami buffer (5 mM Tris·HCl, 1 mM EDTA, 18.5 mM $MgCl_2$ at pH 7.9).

Assembly of the DNA catenane walker to the origami path and monitoring of the transcription by bulk fluorescence experiments

A solution of the catenane walker (final concentration 75 nM) was incubated at room temperature for 15 min with 16 μL of the mastermix (2.5x transcription buffer, RNAsin (1:20 v/v), T7RNAP-ZIF (223 nM), 2.5 mM $MgCl_2$, 18.75% (v/v) DMSO) in order to allow T7RNAP-ZIF (final concentration 86 nM, 1.15 equivalents with respect to catenane) to bind the catenane. In parallel, a solution of the DNA origami nanotube (final concentration 75 nM) was incubated at 37 ºC with the comp-iStep (BHQ-2) ODN (1.33 equivalents per each iStep) or the Step1_blocker ODN for the corresponding control (2 equivalents) for 15 min. Then the catenane and the origami solutions were mixed in 2x DNA buffer (20 mM Tris·HCl, 100 mM NaCl, 20 mM $MgCl_2$ at pH 7.5), adjusting the volume to 40 μL and additionally incubated for 30 min at 37 ºC in order to allow the catenane walker to hybridize to the Step1 position on the DNA origami. The sample was split in two (20 μL each) and loaded in a 386 well plate (ProxiPlate-384 Plus, PerkinElmer). To each well, the NTPs mixture (25 mM, final concentration 2 mM) was added to start transcription and the plate covered with a sealing plastic film (Biorad) to prevent evaporation. Finally, the fluorescence (FAM Ex:492 nm, Em:521 nm; HEX Ex: 535 nm, Em: 556 nm; TAMRA Ex555 nm, Em: 576 nm; Texas Red Ex: 593 nm; Em: 613 nm; Cy5: Ex: 649 nm, Em: 670 nm) was measured in a plate reader (Enspire 2300 (Perkin Elmer) or TECAN Infinite M1000 Pro) every 3 min at 37 ºC for at least 5 h. Analysis of the kinetic data was performed by exponential fitting (one phase decay for Fc fluorophore (TAMRA) and one phase association for Fi fluorophores) using GraphPad Prism software.

Fitting of the data kinetic analysis

One phase decay:

$$FI = (FImax - FImin) \times e^{(-K * X(time))} \quad \text{(Eq. 1)}$$

One phase association:

$$FI = FImin + (FImax - FImin) \times (1 - e^{(-K * X(time))} \quad \text{(Eq. 2)}$$

Quantum dot attachment after transcription

The assembly of the DNA catenane walker to the origami path and subsequent transcription reaction were performed as described previously. To allow the attachment of the streptavidin coated quantum dots (Qdots), the comp-iStep (BHQ2) ODN was replaced by a biotinylated version (bio-comp-iStep), which was added to the catenane:origami complex (4 equivalents per binding site/iStep). After adding the NTPs mixture (final concentration 2 mM), aliquots of 5 μL were taken from each sample at different time points (0, 20, 45 and 150 min). These aliquots were further diluted in 400 μL of 2x DNA buffer, filtered in Amicon Ultra-10K centrifugal filters and washed 4 times with extra 300 μL 2x DNA buffer (3x 7500g for 5 min and 1x 7500g for 20 min). After concentration, 0.4 μL of sample (~6.25 nM; final concentration 1 nM) were mixed with 0.5 μL of streptavidin coated quantum dots (Qdot 655 streptavidin conjugate, Thermo Fischer Scientific (1 μM, final concentration 200 nM)) in 1.5x DNA buffer (total volume 2.5 μL). The sample was incubated for 2h at room temperature (or overnight at 4 ºC) before measuring at the AFM.

AFM sample preparation and imaging

All AFM images were obtained using a Nanowizard 3 (JPK instruments). Images of the DNA catenane, T7RNAP-ZIF and catenane motor were recorded in tapping mode (AC mode) in air. The structures were absorbed onto freshly cleaved mica surface coated with 0.001% polyornithine (30-70 kDa; Sigma-Aldrich). For this, 3 μL of polyornithine were deposited on the freshly cleaved mica for ~1 min, washed 3 times with 200 μL of water and dried with an aero duster. Then, 3 μL of sample (2.5 to 5 nM) were deposited for 1 min, washed and dried again. ACTA probes with silicon tips were used. The high-resolution images were obtained in HyperDrive® mode in liquid (water) following the same protocol, except 400 μL of water were added finally on top of the sample. Ultra-Short Cantilever probes (USC) with high dense carbon tips from NanoWorld were used.

AFM images of the DNA catenane walker attached to the origami path were collected in tapping mode (AC mode) in liquid (water). Again, 3 μL of sample (1 nM) were deposited on freshly cleaved mica untreated or coated with 0.001% (w/v) polyornithine, washed once with 200 μL of water and then, 400 μL of water were added on top of the sample to allow imaging in liquid. Ultra-Short Cantilever probes (USC) with high dense carbon tips (NanoWorld) were used.

Images of the DNA origami path labelled with Qdots were taken in tapping mode in air. Three μL of linear polyethylenimine (PEI, Polysciences Inc.) were deposited during 1 min on freshly cleaved mica, washed three times with 200 μL of water and subsequently dried, for coating the surface. Then, 3 μL of sample (0.25 nM) were loaded on the PEI coated surface for 1 min, washed once (200 μL water) and dried with an aero duster. Imaging was performed using ACTA probes (NanoWorld) with silicon tips. The position of the quantum dots was determined according to the design of the DNA origami path and the relative

Europe PMC Funders Author Manuscripts

distances between the iSteps. Incomplete or overlapped structures were not used for the Qdot quantification.

Gel electrophoresis

Catenane assemblies were analyzed using agarose gel electrophoresis (2.5% agarose gel, 0.5x TAE buffer, 20 min at 180V). Six-helix bundle DNA origami assemblies were run in 2 % agarose gels (0.5x TAE, 10 mM $MgCl_2$) for 1 h at 80 V. All gels were poured from 'Agarose High Resolution' (ROTH), stained with ethidium bromide and visualized by UV irradiation.

Supplementary Material

Refer to Web version on PubMed Central for supplementary material.

Acknowledgements

We thank K. Rotscheidt, V. Vieberg, and D. Keppner for technical assistance, and D. Ackermann, A. Kristofferson, and A. Lange for performing preliminary studies. This work was supported by the Alexander von Humboldt Foundation and the European Research Council (ERC Advanced Grant 267173), the Max-Planck Society, and University of Bonn. N. G. W. acknowledges partial funding by Department of Defense grant W911NF-12-1-0420 and NSF grant DMR-1607854. M. F. expresses particular thanks to Hans Famulok (1932-2017) for his genuine and encouraging interest in this work.

References

1. Schliwa M, Woehlke G. Molecular motors. Nature. 2003; 422:759–765. DOI: 10.1038/nature01601 [PubMed: 12700770]
2. Spetzler D, et al. Single molecule measurements of F1-ATPase reveal an interdependence between the power stroke and the dwell duration. Biochemistry. 2009; 48:7979–7985. DOI: 10.1021/bi9008215 [PubMed: 19610671]
3. Macnab RM. How bacteria assemble flagella. Annu Rev Microbiol. 2003; 57:77–100. DOI: 10.1146/annurev.micro.57.030502.090832 [PubMed: 12730325]
4. Krishnan Y, Simmel FC. Nucleic acid based molecular devices. Angew Chem Int Ed. 2011; 50:3124–3156. DOI: 10.1002/anie.200907223
5. Zhang DY, Seelig G. Dynamic DNA nanotechnology using strand-displacement reactions. Nat Chem. 2011; 3:103–113. DOI: 10.1038/nchem.957 [PubMed: 21258382]
6. Bath J, Turberfield AJ. DNA nanomachines. Nat Nanotechnol. 2007; 2:275–284. nnano.2007.104 [pii]. DOI: 10.1038/nnano.2007.104 [PubMed: 18654284]
7. Ketterer P, Willner EM, Dietz H. Nanoscale rotary apparatus formed from tight-fitting 3D DNA components. Sci Adv. 2016; 2:e1501209.doi: 10.1126/sciadv.1501209 [PubMed: 26989778]
8. van den Heuvel MG, Dekker C. Motor proteins at work for nanotechnology. Science. 2007; 317:333–336. DOI: 10.1126/science.1139570 [PubMed: 17641191]
9. Goel A, Vogel V. Harnessing biological motors to engineer systems for nanoscale transport and assembly. Nat Nanotechnol. 2008; 3:465–475. DOI: 10.1038/nnano.2008.190 [PubMed: 18685633]
10. Giselbrecht S, Rapp BE, Niemeyer CM. The chemistry of cyborgs--interfacing technical devices with organisms. Angew Chem Int Ed. 2013; 52:13942–13957. DOI: 10.1002/anie.201307495
11. Feringa BL. In control of motion: from molecular switches to molecular motors. Acc Chem Res. 2001; 34:504–513. [PubMed: 11412087]
12. von Delius M, Leigh DA. Walking molecules. Chem Soc Rev. 2011; 40:3656–3676. DOI: 10.1039/c1cs15005g [PubMed: 21416072]

13. Fletcher SP, Dumur F, Pollard MM, Feringa BL. A reversible, unidirectional molecular rotary motor driven by chemical energy. Science. 2005; 310:80–82. DOI: 10.1126/science.1117090 [PubMed: 16210531]
14. Wilson MR, et al. An autonomous chemically fuelled small-molecule motor. Nature. 2016; 534:235–240. DOI: 10.1038/nature18013 [PubMed: 27279219]
15. Daubendiek SL, Ryan K, Kool ET. Rolling-Circle RNA Synthesis: Circular Oligonucleotides as Efficient Substrates for T7 RNA Polymerase. J Am Chem Soc. 1995; 117:7818–7819. DOI: 10.1021/ja00134a032 [PubMed: 27524830]
16. Elrod-Erickson M, Rould MA, Nekludova L, Pabo CO. Zif268 protein-DNA complex refined at 1.6 A: a model system for understanding zinc finger-DNA interactions. Structure. 1996; 4:1171–1180. [PubMed: 8939742]
17. Nakata E, et al. Zinc-finger proteins for site-specific protein positioning on DNA-origami structures. Angew Chem Int Ed. 2012; 51:2421–2424. DOI: 10.1002/anie.201108199
18. Ngo TA, Nakata E, Saimura M, Morii T. Spatially Organized Enzymes Drive Cofactor-Coupled Cascade Reactions. J Am Chem Soc. 2016; 138:3012–3021. DOI: 10.1021/jacs.5b10198 [PubMed: 26881296]
19. Lohmann F, Valero J, Famulok M. A novel family of structurally stable double stranded DNA catenanes. Chem Commun. 2014; 50:6091–6093. DOI: 10.1039/c4cc02030h
20. Ackermann D, Jester SS, Famulok M. Design strategy for DNA rotaxanes with a mechanically reinforced PX100 axle. Angew Chem Int Ed. 2012; 51:6771–6775. DOI: 10.1002/anie.201202816
21. Ackermann D, et al. A double-stranded DNA rotaxane. Nat Nanotechnol. 2010; 5:436–442. [PubMed: 20400967]
22. Weigandt J, Chung C-L, Jester S-S, Famulok M. A daisy chain rotaxane interlocked DNA nanostructure. Angew Chem Int Ed. 2016; 55:5512–5516. DOI: 10.1002/anie.201601042
23. Lionberger TA, Meyhofer E. Bending the rules of transcriptional repression: tightly looped DNA directly represses T7 RNA polymerase. Biophys J. 2010; 99:1139–1148. DOI: 10.1016/j.bpj.2010.04.074 [PubMed: 20712997]
24. Lee W, von Hippel PH, Marcus AH. Internally labeled Cy3/Cy5 DNA constructs show greatly enhanced photo-stability in single-molecule FRET experiments. Nucleic Acids Res. 2014; 42:5967–5977. DOI: 10.1093/nar/gku199 [PubMed: 24627223]
25. Yang WP, Wu H, Barbas CF 3rd. Surface plasmon resonance based kinetic studies of zinc finger-DNA interactions. J Immunol Methods. 1995; 183:175–182. [PubMed: 7602135]
26. Ko SH, Gallatin GM, Liddle JA. Nanomanufacturing with DNA Origami: Factors Affecting the Kinetics and Yield of Quantum Dot Binding. Adv Funct Mater. 2012; 22:1015–1023. DOI: 10.1002/adfm.201102077
27. Abendroth JM, Bushuyev OS, Weiss PS, Barrett CJ. Controlling Motion at the Nanoscale: Rise of the Molecular Machines. ACS Nano. 2015; 9:7746–7768. DOI: 10.1021/acsnano.5b03367 [PubMed: 26172380]
28. Pan J, et al. Visible/near-infrared subdiffraction imaging reveals the stochastic nature of DNA walkers. Sci Adv. 2017; 3:e1601600.doi: 10.1126/sciadv.1601600 [PubMed: 28116353]
29. Pan J, Li F, Cha TG, Chen H, Choi JH. Recent progress on DNA based walkers. Curr Opin Biotechnol. 2015; 34:56–64. DOI: 10.1016/j.copbio.2014.11.017 [PubMed: 25498478]
30. Yehl K, et al. High-speed DNA-based rolling motors powered by RNase H. Nat Nanotechnol. 2016; 11:184–190. DOI: 10.1038/nnano.2015.259 [PubMed: 26619152]
31. Tomov TE, et al. DNA Bipedal Motor Achieves a Large Number of Steps Due to Operation Using Microfluidics-Based Interface. Acs Nano. 2017; 11:4002–4008. DOI: 10.1021/acsnano.7b00547 [PubMed: 28402651]
32. Zhang DY, Winfree E. Control of DNA strand displacement kinetics using toehold exchange. J Am Chem Soc. 2009; 131:17303–17314. DOI: 10.1021/ja906987s [PubMed: 19894722]
33. Jung C, Allen PB, Ellington AD. A stochastic DNA walker that traverses a microparticle surface. Nat Nanotechnol. 2016; 11:157–163. DOI: 10.1038/nnano.2015.246 [PubMed: 26524397]
34. Omabegho T, Sha R, Seeman NC. A bipedal DNA Brownian motor with coordinated legs. Science. 2009; 324:67–71. 324/5923/67 [pii]. DOI: 10.1126/science.1170336 [PubMed: 19342582]

35. Berna J, et al. Macroscopic transport by synthetic molecular machines. Nat Mater. 2005; 4:704–710. DOI: 10.1038/nmat1455 [PubMed: 16127455]
36. Kudernac T, et al. Electrically driven directional motion of a four-wheeled molecule on a metal surface. Nature. 2011; 479:208–211. DOI: 10.1038/nature10587 [PubMed: 22071765]
37. Lu CH, Cecconello A, Elbaz J, Credi A, Willner I. A three-station DNA catenane rotary motor with controlled directionality. Nano Letters. 2013; 13:2303–2308. DOI: 10.1021/nl401010e [PubMed: 23557381]
38. Venkataraman S, Dirks RM, Rothemund PW, Winfree E, Pierce NA. An autonomous polymerization motor powered by DNA hybridization. Nat Nanotechnol. 2007; 2:490–494. DOI: 10.1038/nnano.2007.225 [PubMed: 18654346]
39. Turberfield AJ, et al. DNA fuel for free-running nanomachines. Phys Rev Lett. 2003; 90:118102. [PubMed: 12688969]
40. Bath J, Green SJ, Turberfield AJ. A free-running DNA motor powered by a nicking enzyme. Angew Chem Int Ed. 2005; 44:4358–4361. DOI: 10.1002/anie.200501262
41. Lund K, et al. Molecular robots guided by prescriptive landscapes. Nature. 2010; 465:206–210. DOI: 10.1038/nature09012 [PubMed: 20463735]
42. Eelkema R, et al. Molecular machines: nanomotor rotates microscale objects. Nature. 2006; 440:163.doi: 10.1038/440163a [PubMed: 16525460]
43. Liu MH, et al. Biomimetic Autonomous Enzymatic Nanowalker of High Fuel Efficiency. Acs Nano. 2016; 10:5882–5890. DOI: 10.1021/acsnano.6b01035 [PubMed: 27294366]
44. Cheng J, et al. Bipedal nanowalker by pure physical mechanisms. Phys Rev Lett. 2012; 109:238104.doi: 10.1103/PhysRevLett.109.238104 [PubMed: 23368271]
45. Loh IY, Cheng J, Tee SR, Efremov A, Wang Z. From bistate molecular switches to self-directed track-walking nanomotors. ACS Nano. 2014; 8:10293–10304. DOI: 10.1021/nn5034983 [PubMed: 25268955]
46. Bath J, Green SJ, Allen KE, Turberfield AJ. Mechanism for a Directional, Processive, and Reversible DNA Motor. Small. 2009; 5:1513–1516. DOI: 10.1002/smll.200900078 [PubMed: 19296556]
47. Tian Y, He Y, Chen Y, Yin P, Mao C. A DNAzyme that walks processively and autonomously along a one-dimensional track. Angew Chem Int Ed. 2005; 44:4355–4358. DOI: 10.1002/anie.200500703
48. Yang Y, et al. A Photoregulated DNA-Based Rotary System and Direct Observation of Its Rotational Movement. Chemistry. 2017; 23:3979–3985. DOI: 10.1002/chem.201605616 [PubMed: 28199775]
49. Michelotti N, de Silva C, Johnson-Buck AE, Manzo AJ, Walter NG. A bird's eye view tracking slow nanometer-scale movements of single molecular nano-assemblies. Methods Enzymol. 2010; 475:121–148. DOI: 10.1016/S0076-6879(10)75006-0 [PubMed: 20627156]
50. Aitken CE, Marshall RA, Puglisi JD. An oxygen scavenging system for improvement of dye stability in single-molecule fluorescence experiments. Biophys J. 2008; 94:1826–1835. DOI: 10.1529/biophysj.107.117689 [PubMed: 17921203]
51. Fu J, et al. Multi-enzyme complexes on DNA scaffolds capable of substrate channelling with an artificial swinging arm. Nat Nanotechnol. 2014; 9:531–536. DOI: 10.1038/nnano.2014.100 [PubMed: 24859813]
52. Suddala KC, Walter NG. Riboswitch structure and dynamics by smFRET microscopy. Methods Enzymol. 2014; 549:343–373. DOI: 10.1016/B978-0-12-801122-5.00015-5 [PubMed: 25432756]
53. Suddala KC, Wang J, Hou Q, Walter NG. Mg(2+) shifts ligand-mediated folding of a riboswitch from induced-fit to conformational selection. J Am Chem Soc. 2015; 137:14075–14083. DOI: 10.1021/jacs.5b09740 [PubMed: 26471732]
54. Fu J, et al. Assembly of multienzyme complexes on DNA nanostructures. Nat Protoc. 2016; 11:2243–2273. DOI: 10.1038/nprot.2016.139 [PubMed: 27763626]
55. Rashid F, et al. Single-molecule FRET unveils induced-fit mechanism for substrate selectivity in flap endonuclease 1. Elife. 2017; 6doi: 10.7554/eLife.21884

56. Rueda D, et al. Single-molecule enzymology of RNA: essential functional groups impact catalysis from a distance. Proc Natl Acad Sci U S A. 2004; 101:10066–10071. DOI: 10.1073/pnas.0403575101 [PubMed: 15218105]

57. Douglas SM, et al. Rapid prototyping of 3D DNA-origami shapes with caDNAno. Nucleic Acids Res. 2009; 37:5001–5006. DOI: 10.1093/nar/gkp436 [PubMed: 19531737]

58. Stahl E, Martin TG, Praetorius F, Dietz H. Facile and scalable preparation of pure and dense DNA origami solutions. Angew Chem Int Ed Engl. 2014; 53:12735–12740. DOI: 10.1002/anie.201405991 [PubMed: 25346175]

Europe PMC Funders Author Manuscripts

Europe PMC Funders Author Manuscripts

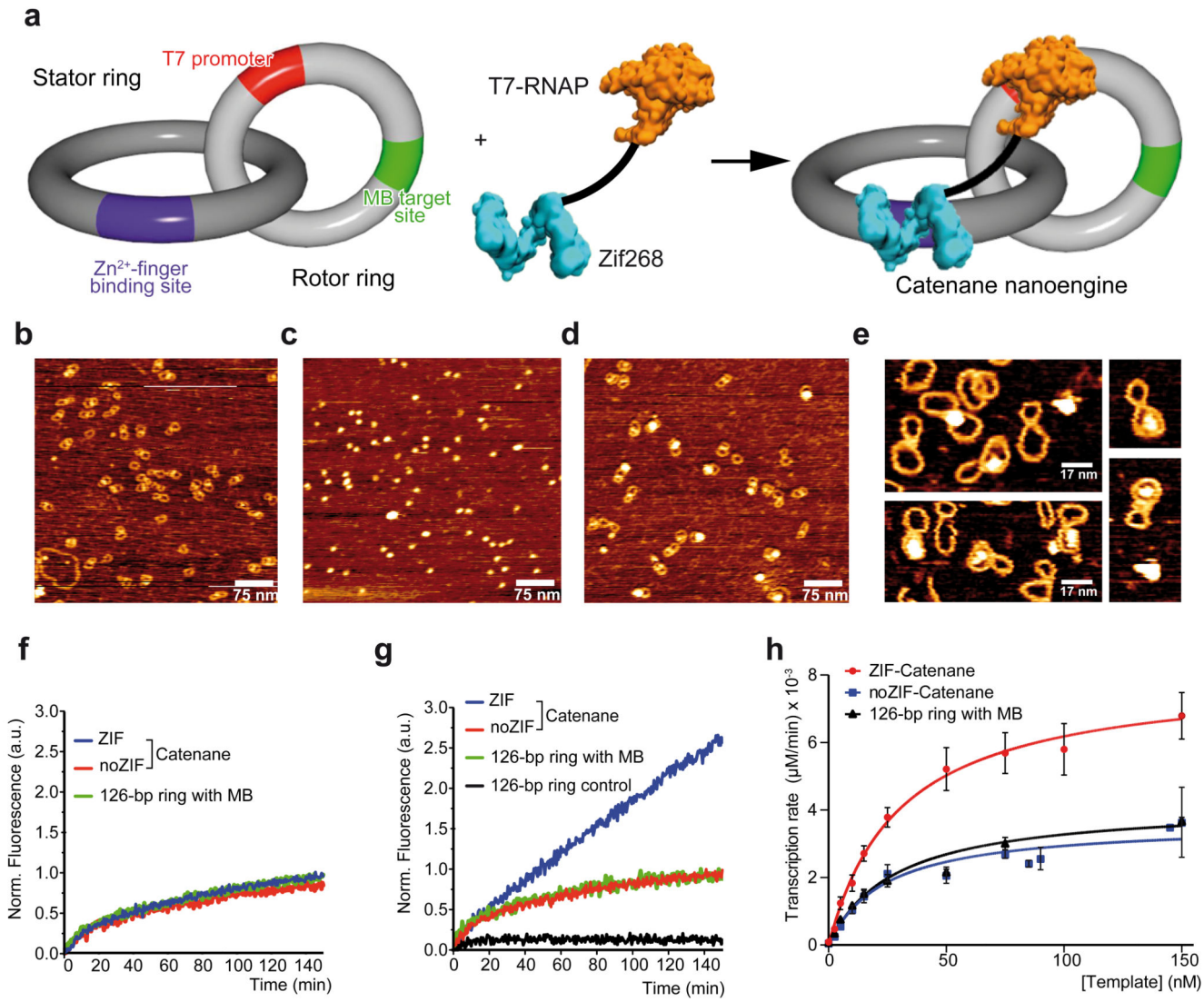

Figure 1. Assembly of the DNA catenane rotary motor.

(**a**) Schematic representation of T7RNAP-ZIF protein assembled on the DNA catenane. (**b**) AFM imaging in tapping mode in air of catenane, (**c**) T7RNAP-ZIF and (**d**) catenane – T7RNAP-ZIF assembly. (**e**) HR-AFM images of the catenane- T7RNAP-ZIF nanoengine in tapping mode in liquid. (**f**, **g**) Fluorescence kinetics of the RCT performed by the catenane (blue), control catenane lacking the Zif268 binding site (red), a positive control double stranded 126-bp ring (green) and a negative control 126-bp ring (black) in the presence of wild-type T7RNAP (**f**) and T7RNAP-ZIF (**g**), respectively. (**h**) Transcription rate analysis at different concentrations of catenane (red), catenane control (blue) and ring positive control (black) after 150 min of transcription. Error bars: n = 2, mean ±SD

Europe PMC Funders Author Manuscripts

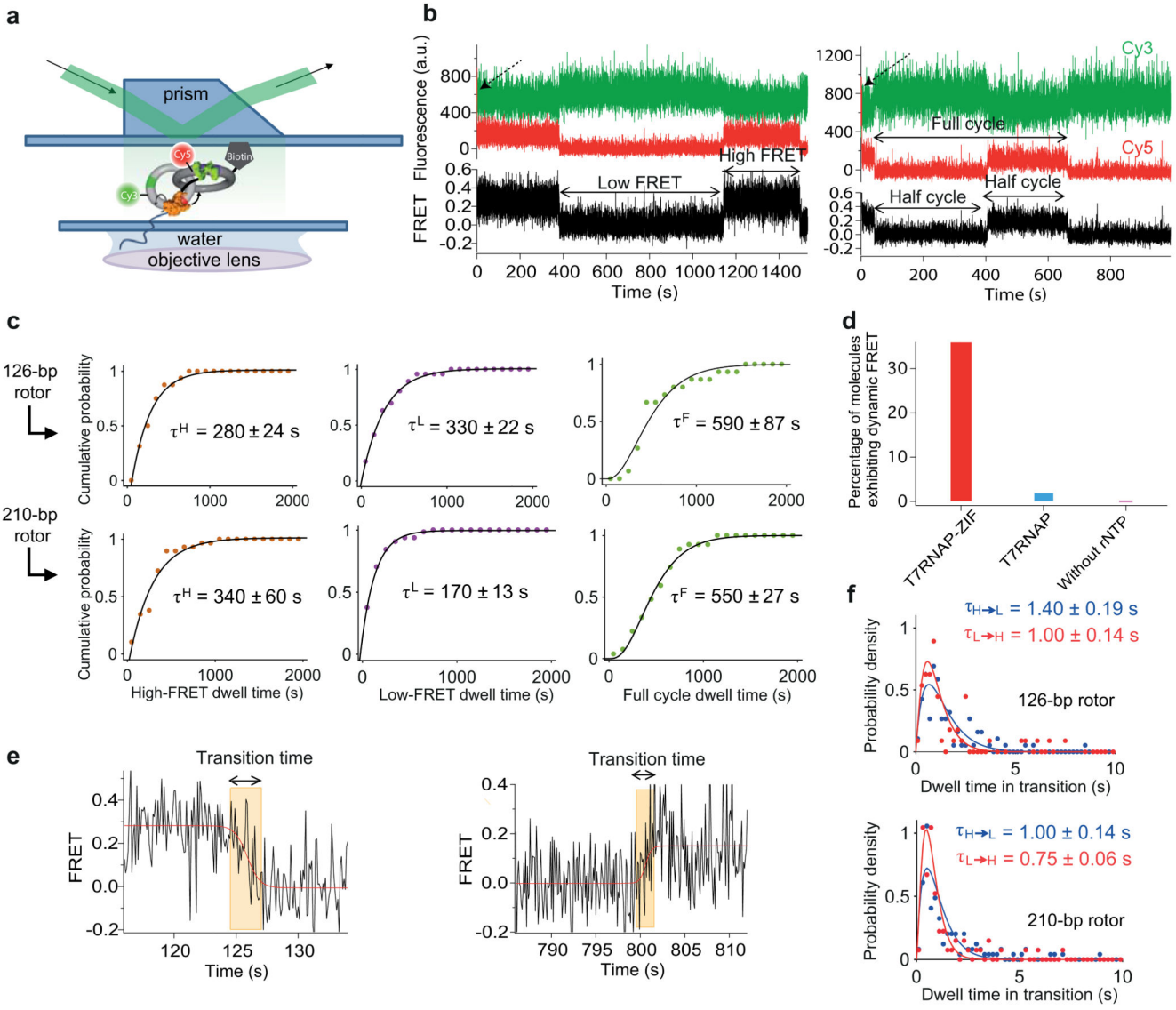

Figure 2. Single-molecule FRET studies of the DNA catenane rotatory motor.

(**a**) Schematic representation of the experimental set-up used for the smFRET studies. (**b**) Representative dynamic trajectories from smFRET experiments showing low- and high-FRET states (left panel) and full and half transcription cycles (right panel). Green and red lines represent the fluorescence intensity of the Cy3 donor and Cy5 acceptor, respectively, whereas the black line represents the resulting FRET signal. The presence of Cy5 was confirmed at the very beginning of the data collection by direct excitation with a 640 nm laser (black broken arrow). (**c**) Transcription cycle kinetics were obtained from the smFRET data for the nanoengine with the 126-bp rotor (upper panels) and the 210-bp (lower panels) by exponential fitting of the cumulative distribution of the dwell times in the high- and low-FRET states (left and middle panel), whereas that for the full transcription cycle (right panel) was calculated from a fit with a Gamma function assuming *n* irreversible steps with identical rates. The dwell times were corrected for the limited observation time window. The

dwell times in the high- and low-FRET states were calculated from 15-44 molecules. (**d**) Percentage of molecules exhibiting dynamic FRET in the presence of T7RNAP-ZIF (red), wild-type T7RNAP (blue), and in the absence of NTPs (magenta). (**e**) Representative trajectories of the transition times from high- to low-FRET state and vice versa (left and right panels, respectively). The time each transition covers was extracted and probability densities of these transition times calculated. The red lines serve only as visual guides. (**f**) Probability density distributions of the transition times obtained from 30 and 90 smFRET trajectories for the catenanes with the 126-bp rotor (left panel) and the 210-bp rotor (right panel), respectively, were fitted with Gamma functions to obtain the underlying time constants.

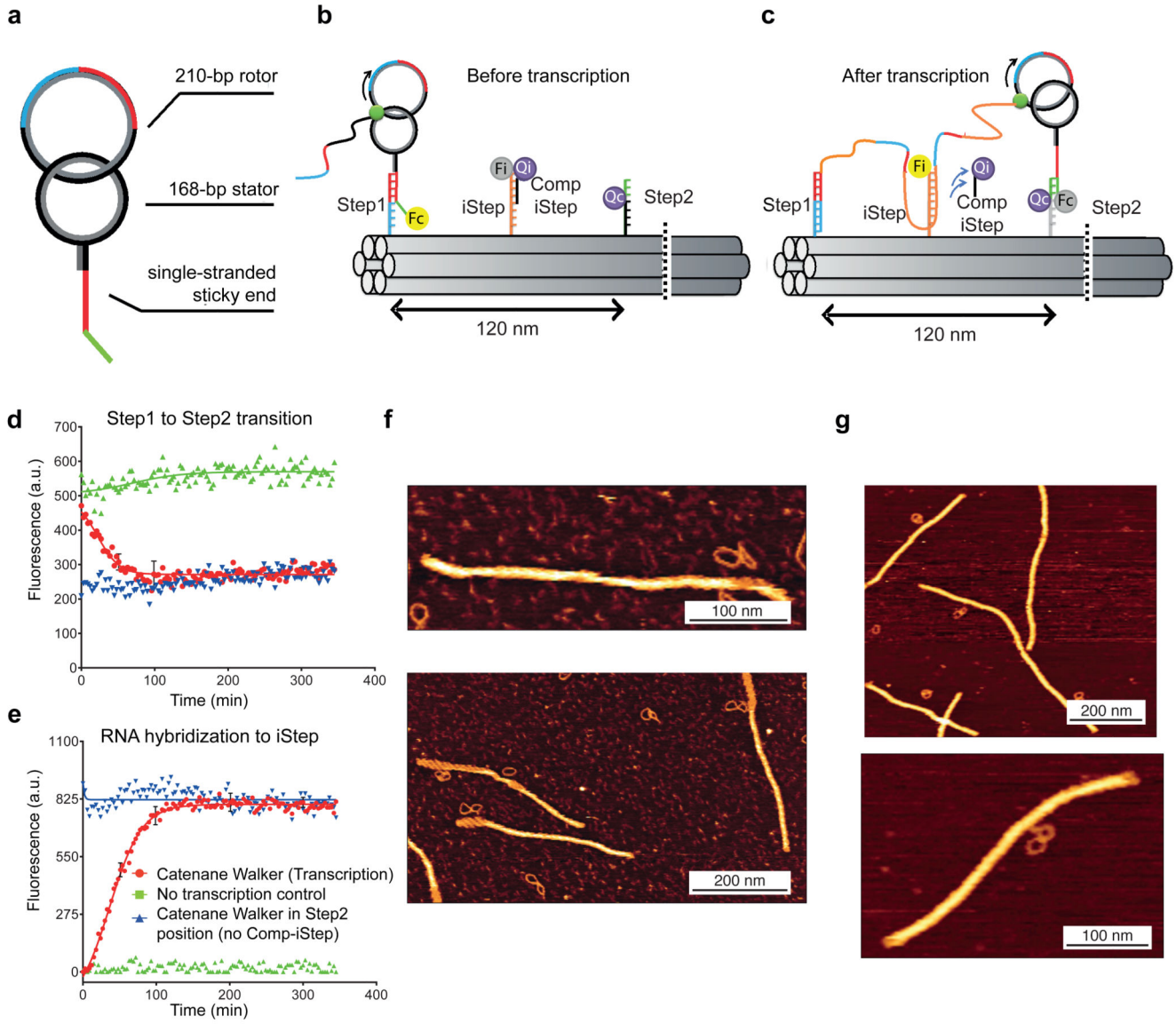

Figure 3. The nanoengine moves along predefined tracks.

(**a**) Scheme of the DNA catenane walker bearing a single stranded sticky end for the specific hybridization to Step1 or Step2 on a predefined DNA path. (**b**, **c**) Scheme of the working principle of the DNA catenane walker on a six helix-bundle DNA origami path before (**b**) and after (**c**) transcription. Fc: TAMRA; Fi: Cy5; Qi and Qc: Black hole quencher 2 (BHQ2). Green circle: T7RNAP-ZIF. (**d**, **e**) Kinetic fluorescence analysis of the catenane:DNA path assembly in presence or in absence of transcription (red and blue lines, respectively) and the corresponding controls (green lines) for the TAMRA fluorophore (Fc) attached to the DNA walker (**d**) or the Cy5 fluorophore (Fi) attached to the intermediate step (**e**). (**f**, **g**) AFM imaging in tapping mode in liquid of the DNA catenane walker attached to the initial Step1 (**f**) and final Step2 (**g**) positions of the DNA origami path.

Europe PMC Funders Author Manuscripts

Europe PMC Funders Author Manuscripts

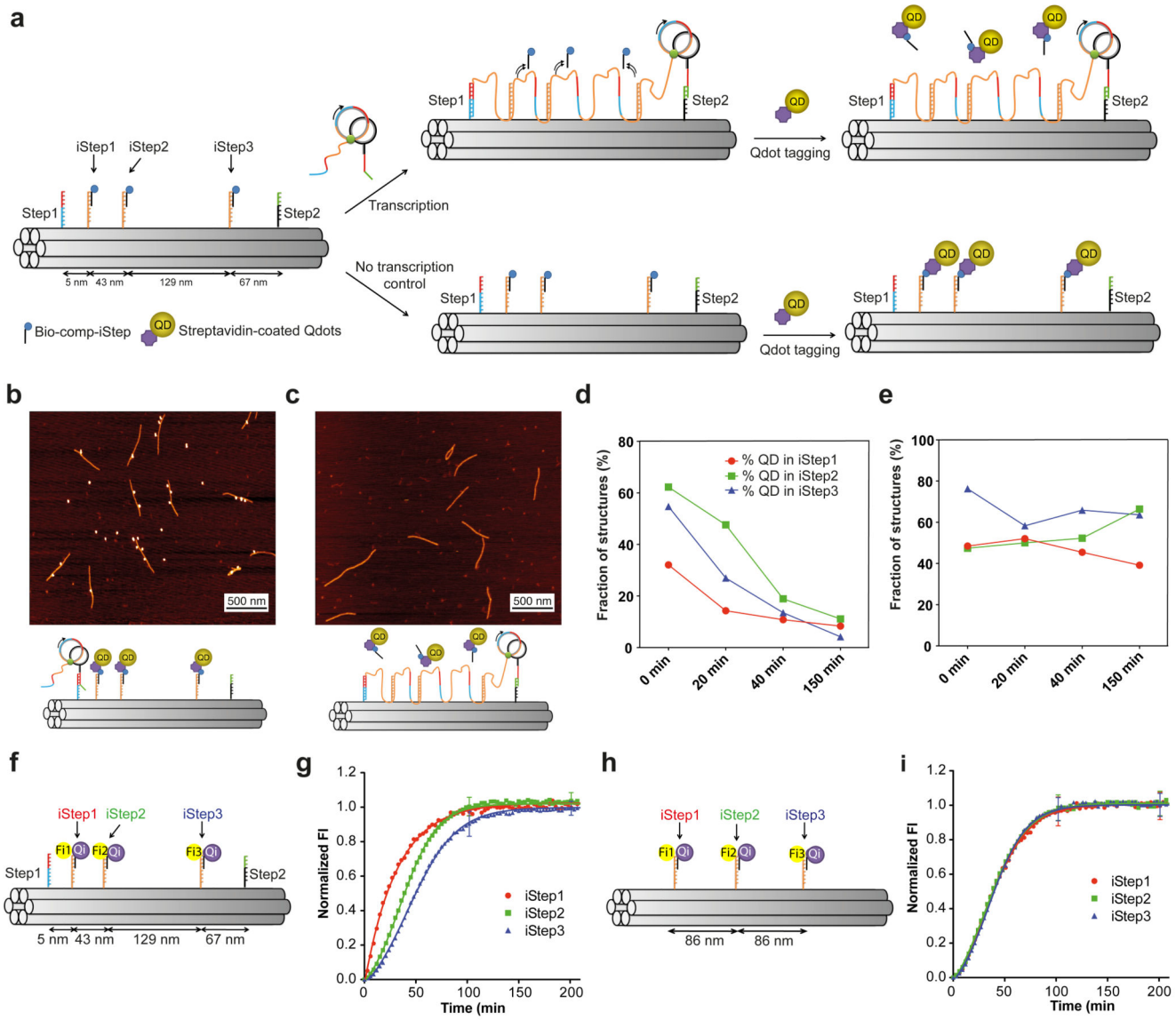

Figure 4. AFM analysis of the RNA sequential hybridization to iSteps during RCT of the catenane walker.

(**a**) Scheme of the origami design, the position and relative distances between iSteps for Qdot tagging. After incubation (37ºC) at different time points in presence or in absence (no transcription control) of the catenane nanoengine, the samples were tagged with the strep-Qdots and analyzed by AFM. (**b, c**) Overall AFM image of the origami tagged with Qdots in the presence of the catenane walker before (**b,** n=443) and after (**c**) transcription. (**d, e**) Qdot occupancy for each origami position at 0, 20, 40, and 150 min on an average of n = 76 structures for each time point in presence (**d**) or in absence (non-transcription control **e**) of the catenane walker. (**f**) Representation of the DNA origami path labelled with three different fluorophores for each iStep position (Fi1:HEX; Fi2:Cy5; Fi3:Texas Red) (**g**) Fluorescence kinetic data of the RNA hybridization to iStep1 (red), iStep2 (green) and iStep3 (blue) positions upon RCT of the catenane walker (Error bars: n = 4, mean ±SD). (**h**)

Representation of corresponding DNA origami control having equidistant iSteps and lacking Steps 1 and 2 (Fi1:HEX; Fi2:FAM; Fi3:Cy5). (**i**) Fluorescence kinetic data of the RNA hybridization to iStep1 (red), iStep2 (green) and iStep3 (blue) positions in a control DNA origami lacking Step 1 and 2 (**h**), upon RCT of the catenane walker. Half-life (**τ**) values were obtained by exponential fitting of the kinetic fluorescence data. Error bars: n = 4, mean ±SD

Europe PMC Funders Author Manuscripts

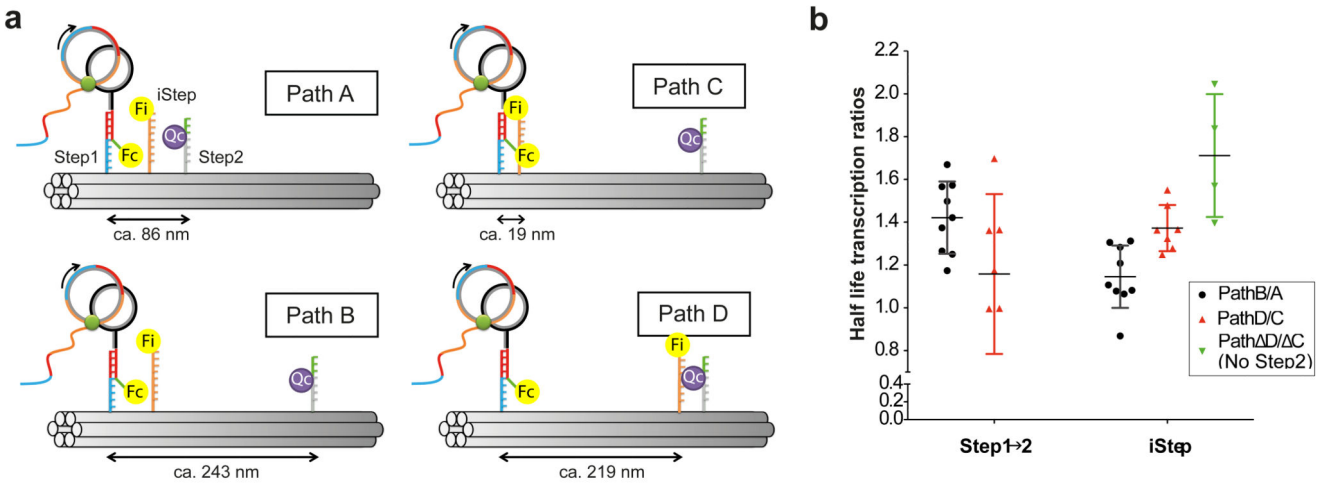

Figure 5. Kinetics of nanoengine walking on a path with varying Distances between steps.

(**a**) Schematic representation of different 6HB DNA origami paths used to evaluate the kinetics of the catenane walker by varying the relative distances between iSteps and Step2 with respect to initial Step1. (**b**) Half-life transcription ratios of the Step 1 to 2 transition and the RNA hybridization to iStep measured for different origami paths. Half-life (**τ**) values were calculated by exponential fitting of the kinetic fluorescence data (Error bars: n=18 for paths A and B, n=14 for paths C and D and n=8 for paths ΔC and ΔD).

Europe PMC Funders Author Manuscripts